J. Ocean Univ. China (Oceanic and Coastal Sea Research)
https://doi.org/10.1007/s11802-021-4554-1
ISSN 1672-5182, 2021 20 (4): 848-856
http://www.ouc.edu.cn/xbywb/
E-mail:xbywb@ouc.edu.cn

Comparison and Calibration of Elemental Measurements in Sediments Using X-Ray Fluorescence Core Scanning with ICP Methods: A Case Study of the South China Sea Deep Basin

XU Fangjian[1), 2)], HU Bangqi[2), 3), 4), *], WANG Chen[1)], ZHAO Jingtao[2), 3)], WANG Feifei[2), 3)], DING Xue[2), 3)], LI Qing[2), 3)], and GUO Jianwei[2), 3)]

1) *School of Geosciences*, *China University of Petroleum*, *Qingdao* 266580, *China*
2) *Laboratory for Marine Mineral Resources*, *Qingdao National Laboratory for Marine Science and Technology*, *Qingdao* 266071, *China*
3) *Qingdao Institute of Marine Geology*, *Ministry of Natural Resources*, *Qingdao* 266071, *China*
4) *State Key Laboratory of Loess and Quaternary Geology*, *Institute of Earth Environment*, *Chinese Academy of Sciences*, *Xi'an* 710075, *China*

(Received April 9, 2020; revised June 16, 2020; accepted July 15, 2020)

Abstract The X-ray fluorescence (XRF) core scanning method is widely applied in studies of sedimentary paleoenvironments due to its convenient pretreatment, nondestructive characteristics, fast execution, continuous scanning, and high resolution. XRF core scanning for sediments is commonly used in the studies on the South China Sea. This study compares XRF-scanned intensities and measured inductively coupled plasma (ICP) elemental contents of core CS11 in the northeast South China Sea deep basin. The results show that the analyzed elements can be separated into three classes. Class I includes elements with high correlation coefficients, such as Ca, Sr, and Zr; Class II contains elements with average correlation coefficients, such as Fe, Mn, Ti, and Cu; and Class III comprises elements with low correlation coefficients, such as K, Ni, Zn, Rb, and Al. In the South China Sea deep basin, pore water, compaction, and grain size have weak effects on the elemental intensities and contents of short core sediments. Hence, for elements with high correlation coefficients, a linear relationship model can be established by the least-squares method, in which the converted XRF intensities are approximately equal to the measured ICP contents. Based on the established log-ratio calibration model, the resulting ln(K/Ca), ln(Ti/Ca), ln(Fe/Ca), and ln(Zr/Ca) values generally display the same variation trends as the measured curves. The elemental contents and ratios produced by the linear model *via* the least-squares method and the log-ratio calibration model are expected to provide high-resolution data support for future paleoenvironmental research on the South China Sea deep basin.

Key words sediment; XRF core scanning; element; deep sea; South China Sea

1 Introduction

The geochemical elemental compositions of sediments, which contain rich information on paleoenvironmental changes, have an excellent application potential in sedimentological and paleoenvironmental studies (Norris and Röhl, 1999; Haschke, 2006; Yao *et al.*, 2010; Boyle *et al.*, 2015; Liu *et al.*, 2017a, 2017b, 2018). Traditional analytical and testing methods for geochemical elements, such as inductively coupled plasma optical emission spectrometry (ICP-OES), also referred to as inductively coupled plasma atomic emission spectrometry (ICP-AES), inductively coupled plasma mass spectrometry (ICP-MS), and X-ray fluorescence (XRF) spectrometry, are subject to various limitations. For example, they require ample time for a sample pretreatment, they are destructive to samples, and the testing is expensive. In addition, these methods are constrained by the sample quantity and division techniques (Croudace and Williams-Thorpe, 1988; Croudace *et al.*, 2006). XRF core scanning, which can directly scan untreated sediment cores, is a good alternative to conventional testing approaches owing to its fast, continuous, high-resolution, and nondestructive nature. However, its scanning results are elemental intensities, which are semi-quantitative and cannot directly represent elemental contents (Janssens *et al.*, 2000; Kido *et al.*, 2006; Weltje and Tjallingii, 2008; Lei *et al.*, 2011; Löwemark *et al.*, 2011; Hennekam and de Lange, 2012). Previous research has compared the results from XRF core scanning with those from traditional fluorescence testing and ICP measure-

* Corresponding author. Tel: 0086-532-85713135
E-mail: bangqihu@gmail.com

ments of sediments. These studies indicate that the XRF scanning results for K, Ca, and Ti can represent their relative content variations (Ge *et al.*, 2005; Kido *et al.*, 2006; Richter *et al.*, 2006; Tjallingii *et al.*, 2007) despite some errors, and the XRF results are reliable after calibration (Tjallingii *et al.*, 2007; Weltje and Tjallingii, 2008). Therefore, a correct understanding and treatment of these elemental intensities is a prerequisite for the effective utilization of XRF results.

Furthermore, researchers have discovered that the energy intensity of X-rays and the physiochemical properties of sediments affect measurement results (Liang *et al.*, 2012; Zhou *et al.*, 2013). The carbonate concentrations in sediments can weaken XRF intensities (Kuhlmann *et al.*, 2004). Water contents can significantly weaken the intensities of Al and Si (Kido *et al.*, 2006; Tjallingii *et al.*, 2007) but are less influential on K, Ti, Fe, and Ca (Tjallingii *et al.*, 2007). Accordingly, methods have been tested to mitigate the effect of the sample roughness and density by increasing the scanned area of sediment samples (Janssens *et al.*, 2000). Al, as the lightest element detectable by this method, can be used as a tool to calibrate the intensity errors of heavy elements, which are caused by organic carbon or carbonate enrichment (Löwemark *et al.*, 2011). Cl, an important constituent of seawater, can be used as an indicator for the water content in marine sediments to calibrate the intensity errors of light elements associated with the water content (Tjallingii *et al.*, 2007; Hennekam and de Lange, 2012; Chen *et al.*, 2016). Studies have demonstrated that XRF-scanned intensities can be linearly correlated with elemental contents (Jansen *et al.*, 1998; Philipp *et al.*, 2007). Lei *et al.* (2011) established a linear relationship by combining XRF results with ICP-OES measurements using the least-squares method and applied this model to convert elemental intensities into elemental contents. Weltje and Tjallingii (2008) proposed that calibrations with log ratios or multivariate log ratios can be used to quantitatively convert XRF intensities into elemental contents. Lyle *et al.* (2012) estimated the geochemical elemental contents in sediments with a normalized median-scaled method. Recently, Chen *et al.* (2016) presented a polynomial water content calibration approach that combines both methods. They recommended that either of the two methods can be applied for the paleoenvironmental studies of major elements measured by XRF scanning in long sediment sequences.

The South China Sea is a typical marginal sea in the Western Pacific Region, with an average water depth of more than 1000 m. It is a semiclosed sea basin and has significant ramifications on paleoenvironmental and paleoclimatic research. To date, studies on the South China Sea have mostly focused on continental shelves and slopes (Wan *et al.*, 2006; Wang *et al.*, 2014; Gao *et al.*, 2015; Liu *et al.*, 2016), and only little research on deep-sea sediments has been reported. In the present study, we analyzed core CS11 in the South China Sea deep basin using an XRF scanning system. We also tested major and trace elements with the traditional ICP-AES and ICP-MS techniques. We then calibrated the results using the least-squares method and a log-ratio calibration equation. Our findings are expected to provide useful evidence for measuring the elemental contents of sediments in the South China Sea deep basin.

2 Materials and Methods

Sediment core CS11, with a total sample length of 400 cm, was collected from the South China Sea deep basin (118.52°E, 19.03°N, with a water depth of 3755 m).

Samples for the grain size analysis were collected at an interval of 2 cm; 10 mL of 10% HCl and 10 mL of 10% H_2O_2 were added to remove carbonates and organic matter, respectively. After sitting for 12 h, 10 mL of 0.05 mol L^{-1} $(NaPO_3)_6$ was added. The sediment grain sizes were then analyzed using the Malvern Panalytical Mastersizer 2000 laser analyzer. The major (Ca, Fe, Ti, K, Mn, and Al) and trace (Cl, Rb, Cu, Sr, Zn, Zr, and Ni) elements in the sediment core were scanned with a GEOTEK Multi-Sensor Core Logger-XRF high-resolution X-ray core scanner. A total of 102 samples were collected at 2–4 cm intervals for the elemental analysis. The samples were dried at 60℃ and then ground to a 200-mesh screen. A total of 40 mg of each sample was placed in a Teflon vessel, and 1.5 mL of HF and 0.5 mL of HNO_3 were added. The samples were then heated at 150℃ for 12 h. After the sample was fully dissolved, it was diluted to 40 g with deionized water. The major elements were measured with the Thermo Scientific iCAP 6300 ICP-AES system, and the trace elements were measured with a PerkinElmer ELAN DRC II ICP-MS system at the Institute of Oceanology, Chinese Academy of Sciences. The certified Chinese reference materials (GBW 07315 and GBW07316) and United States Geological Survey reference materials (BCR-2 and BHVO-2) were used for quality control.

3 Results

According to the sediment classification standard, the core sediments are mainly clayey silt. The mean grain size (Mz) of the sediments averaged 6.9 φ, with very small vertical variations (Fig.1). The elemental intensities from the XRF scanning were highly variable, ranging from $n\times10^4$ cps for Ca, Fe, and K to $n\times10^2$ cps for Ni. In the ICP tests, the Ca contents were 1%–8%, with an average of 3%; the Fe contents were 3.8%–6.9%, with an average of 5.8%; Ti had low contents of 0.45%–0.76%, with an average of 0.67%; the Sr contents were 125–333 mg kg^{-1}, with an average of 185 mg kg^{-1}; and the Zr contents were 108–202 mg kg^{-1}, with an average of 140 mg kg^{-1}. As shown in Fig.1, Ca, Sr, and Zr showed a strong agreement in their vertical variations, with correlation coefficients (focusing on the ICP-measured layers) of 0.62–0.79; Fe, Mn, Ti, and Cu showed a relatively high agreement in their vertical variations, with correlation coefficients of 0.41–0.58; K, Ni, Zn, and Rb had the lowest agreements in their vertical variations, with correlation coefficients of 0.12–0.30; and Al was slightly negatively correlated.

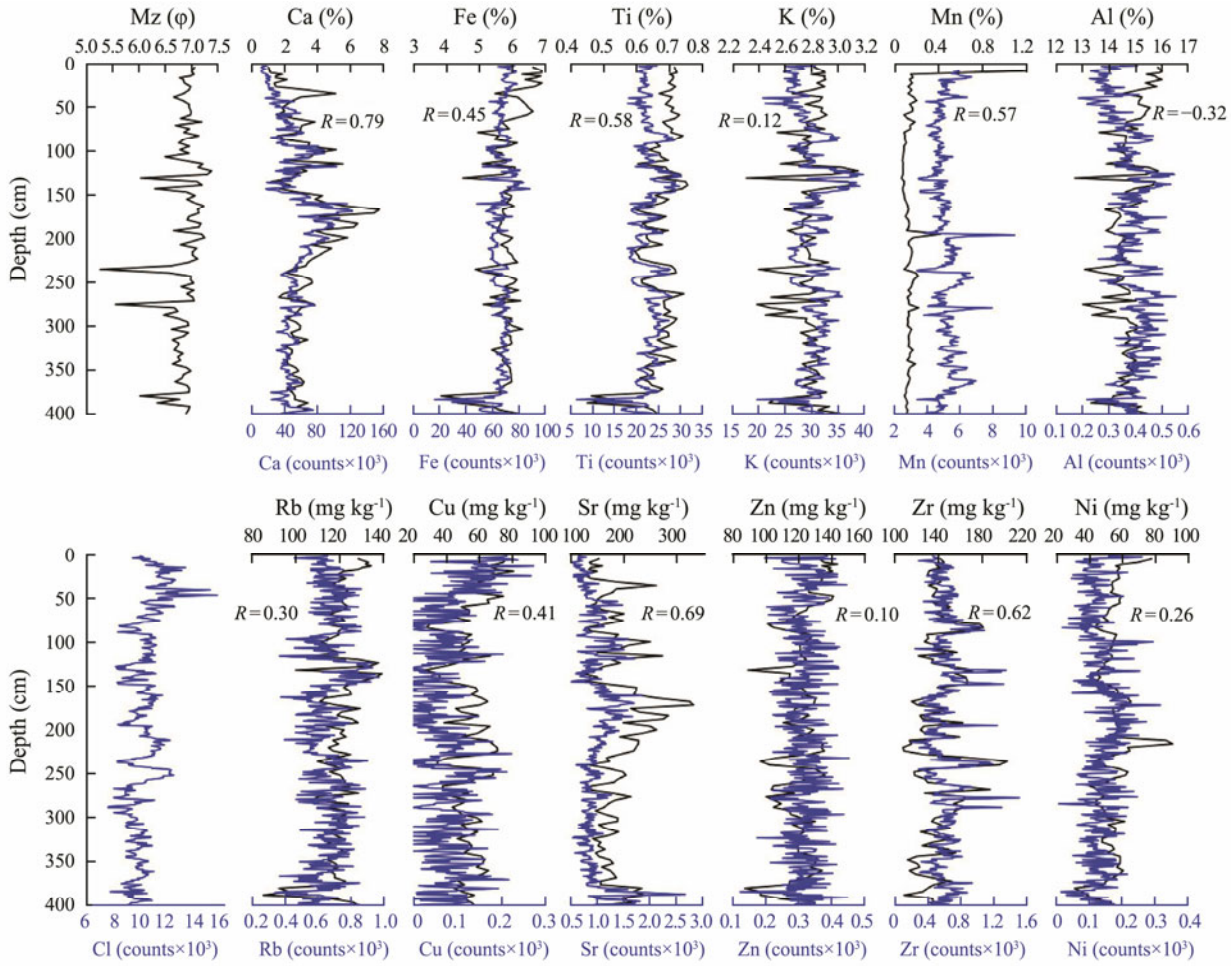

Fig.1 Comparison of the XRF scanning data (blue lines) and conventional ICP concentrations (black lines) of elements with their grain size in the sediments of core CS11.

4 Scanning Ability and Factors Influencing the XRF Intensity

4.1 XRF Scanning Ability

The comparison results of the XRF scanning data and conventional ICP concentrations of elements show that the two methods have a complex correlation. Accordingly, the elements can be divided into three groups. Class I includes elements with high correlation coefficients, such as Ca, Sr, and Zr. Good linear relationships were found between the XRF scanning results and measured ICP results, with correlation coefficients greater than 0.6. In the absence of the measured concentrations, this class of element can be used to replace the ICP method to monitor the variation trend of the elements. Class II contains elements with moderate correlation coefficients, such as Fe, Mn, Ti, and Cu. Relatively good linear relationships were found between the XRF scanning results and measured ICP results, with correlation coefficients between 0.4 and 0.5. In the absence of measured concentrations, this class of element can only be used as an important reference of the ICP method to reflect the variation trend of the elements. Class III comprises elements with low correlation coefficients, such as K, Ni, Zn, Rb, and Al. The linear relationships between the XRF scanning results and the measured ICP results are poor, with correlation coefficients only between 0.1 and 0.3. Significant differences were found in the variation trends of the two results without comparability. The XRF scanning results of such elements do not have much reference value for geochemical analyses.

4.2 Factors Influencing the XRF Intensity

Previous studies have indicated that the main factors influencing XRF measurements include the water content, grain size, and compaction; grain size variations can result in porosity variations and consequently affect the water content of sediments; and compaction can affect the porosity development and eventually affect the water content (Zhang *et al.*, 2013; Zhou *et al.*, 2013). Furthermore, the core sediments are mainly clayey silt. The mean grain size of the sediments showed very small vertical variations except for a few abnormal coarse layers (Fig.1). Thus, the influence of the porosity change caused by the grain size on the variation in the water content should not be significant. Although the XRF core scanning and ICP analysis differ in terms of their testing principles and forms of presentation, both methods have variations in the ele-

mental contents (Wei *et al.*, 2004). Ideally, the ratios between the results of the two methods should be vertically constant. Hence, we used the ratios between the measurements from the two methods to further investigate the causes behind the elemental content variations. This ratio, expressed as $R_{(XRF/ICP)}$, is calculated as follows:

$$R_{(XRF/ICP)} = \text{Element}_{XRF} / \text{Element}_{ICP}, \quad (1)$$

where Element_{XRF} and Element_{ICP} are the elemental intensities from the XRF scanning and the elemental contents from the ICP measurements, respectively. Considering the highly variable ratios of the individual elements, we normalized all ratios using the min-max standardization method (Zhu and Xu, 2003):

$$X^* = (X - \min)/(\max - \min). \quad (2)$$

The element Cl, as an important constituent of seawater, is often used as a proxy for pore water (Tjallingii *et al.*, 2007). As shown in Fig.1, the intensity of Cl decreases as the depth increases, suggesting that Cl can be used as a proxy for pore water. Theoretically, as the depth increases, the pressure and compaction increase and the pore water decreases, so the contents of other elements per unit volume and their corresponding intensities and the $R_{(XRF/ICP)}$ value should also increase. However, as the Cl intensity is poorly correlated with $R_{(XRF/ICP)}$ (generally $R<0.2$), the water content has a weak effect on the XRF intensity. As shown in Fig.2, $R_{(XRF/ICP)}$ is poorly correlated with the core depth, suggesting that compaction also has a weak effect on the XRF intensities. This result can be attributed to the length of the sediment core CS11, which is only 4 m long. Although the sediments were exposed to greater pressures at the bottom than at the top, with a water depth of 3755 m, the pressure difference over 4 m can be ignored. Similarly, the correlations between the intensities and contents for the element and mean grain size are small (Table 1), further verifying the previous argument. Hence, the water content, compaction, and grain size have weak effects on the XRF intensities and elemental contents of the sediments from core CS11.

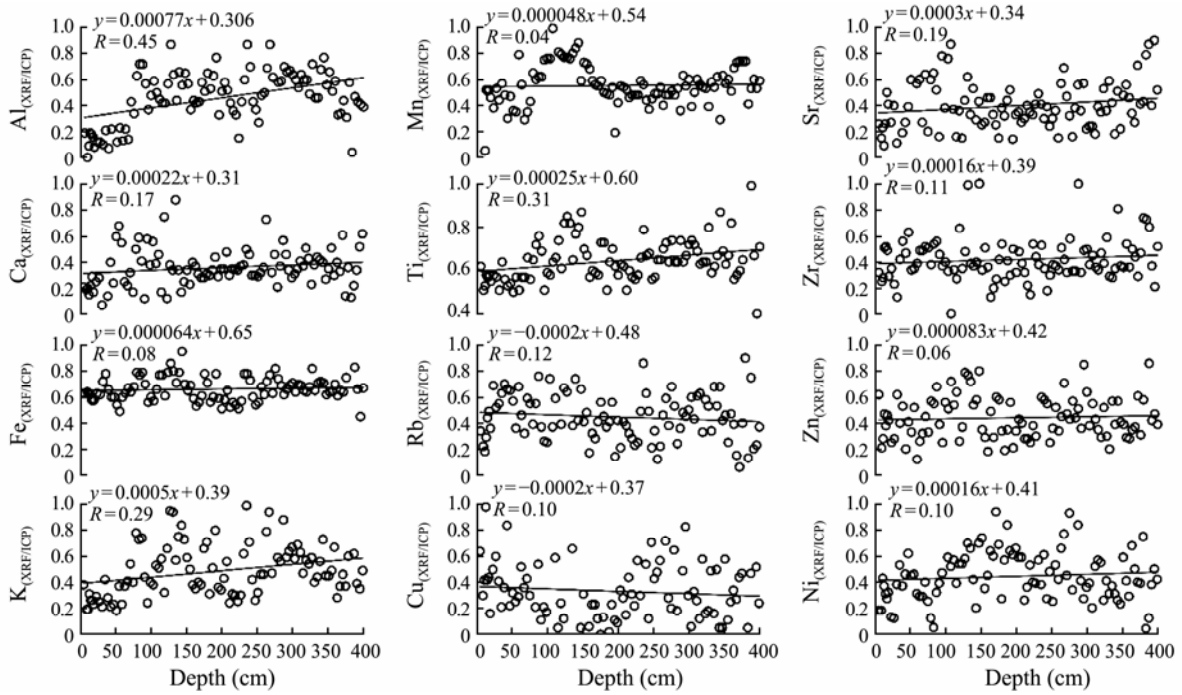

Fig.2 Vertical variation in the ratio of the intensities and concentrations ($R_{(XRF/ICP)}$) of the sediments from core CS11.

Table 1 Correlations between the sediment mean grain size and the measured element concentrations in the core CS11 sediments

Element	CaO	Fe_2O_3	TiO_2	K_2O	MnO	Al_2O_3	Rb	Cu	Sr	Zn	Zr	Ni
Fe_2O_3	−0.28											
TiO_2	−0.49	0.51										
K_2O	−0.26	0.63	0.30									
MnO	−0.23	0.32	0.12	0.07								
Al_2O_3	−0.42	0.77	0.43	0.89	0.28							
Rb	−0.26	0.70	0.70	0.69	0.18	0.69						
Cu	0.16	0.55	−0.30	0.23	0.37	0.39	0.03					
Sr	0.95	−0.33	−0.63	−0.26	−0.13	−0.38	−0.35	0.25				
Zn	0.08	0.78	0.07	0.50	0.23	0.61	0.41	0.83	0.06			
Zr	−0.41	−0.20	0.65	−0.26	−0.03	−0.19	0.17	−0.73	−0.50	−0.59		
Ni	0.27	0.52	−0.08	0.17	0.39	0.24	0.22	0.69	0.24	0.75	−0.49	
Mean grain size	0.21	0.48	0.07	0.53	0.11	0.51	0.46	0.36	0.17	0.53	−0.39	0.37

5 XRF Scanning Result Calibration Model

5.1 Linear Computational Model for the XRF Scanning Results

We established a linear regression equation for the elements with high XRF intensities and content correlations (Classes I and II) based on the least-squares linear regression of Lei *et al.* (2011):

$$\begin{cases} \mathrm{Ca_{ICP}} = 0.048 \times \mathrm{Ca_{XRF}} + 0.721,\ R = 0.79 \\ \mathrm{Fe_{ICP}} = 0.029 \times \mathrm{Fe_{XRF}} + 3.938,\ R = 0.45 \\ \mathrm{Ti_{ICP}} = 0.01 \times \mathrm{Ti_{XRF}} + 0.449,\ R = 0.59 \\ \mathrm{Sr_{ICP}} = 113.196 \times \mathrm{Sr_{XRF}} + 79.386,\ R = 0.70 \\ \mathrm{Zr_{ICP}} = 61.972 \times \mathrm{Zr_{XRF}} + 102.815,\ R = 0.62 \end{cases}, \quad (3)$$

where the ICP values of Ca are expressed in %, the ICP values of Sr and Zr are expressed in $\mathrm{mg\,kg^{-1}}$, and the XRF intensities of individual elements are the original intensities multiplied by 10^{-3}.

In previous studies, calibrations have usually been conducted for pore water and compaction. To further determine whether compaction affected the XRF measurements, we used the linear relationships between the elemental ratios from the two methods and depths to calibrate compaction effects (Zhang *et al.*, 2013). Using the midpoint of the sediment core as the base point, we calibrated the results for Ca, Sr, Zr, Fe, and Ti using the following equation:

$$Y' = Y - k\Delta x, \quad (4)$$

where Y and Y' are the values before and after calibration, respectively; k is the slope of the elemental ratio as a function of depth (the exact value varies from one element to another); and Δx is the distance from the calibration depth to the base point. After the compaction calibration, the correlations of the five elements with the ICP measurements slightly changed; the correlations of Ca, Sr, and Zr slightly increased, whereas those of Fe and Ti remained basically unchanged (Fig.3). Overall, after the compaction calibration, the improvements in the correlations of the elemental contents between the XRF scanning and ICP measurements were not significant. This result agrees with previous results that, with a high overall hydraulic pressure, compaction has weak effects on the top and bottom parts of the analyzed sediments.

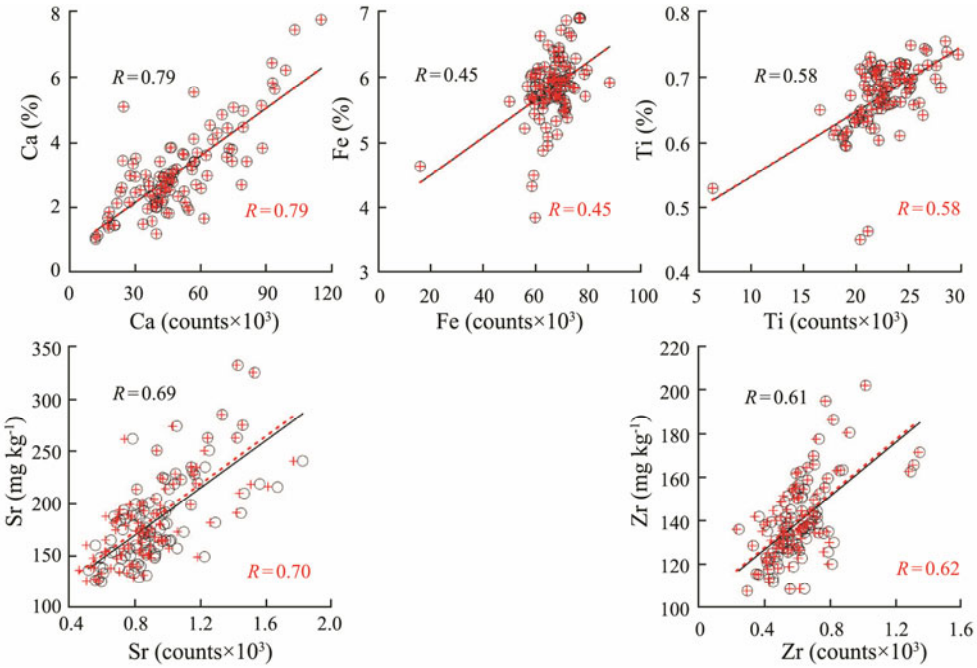

Fig.3 Relationship between the elemental concentrations and intensities before and after compaction calibration. The black dots represent the original data, and the red crosses represent the data after compaction calibration.

Based on the linear regression equation calculated by the least-squares linear regression, we calculated the variations in the vertical contents for Ca, Sr, and Zr in Class I and Fe and Ti in Class II, which showed relatively good correlations. The results fairly agree well with the ICP measurements, especially for the elements in Class I (Fig.4). The variations in Fe and Ti show slight deviations, but the general variation trend could be used as a reference. Hence, for short sediment cores from deep-sea environments (such as the South China Sea deep basin), XRF intensities and elemental contents with good correlation coefficients may be used for conversion.

5.2 Log-Ratio Calibration Model for the XRF Scanning Results

Neither a single-element linear model nor the least-squares linear regression could completely correct the errors resulting from organic matter and other matrix effects (Weltje and Tjallingii, 2008; Pang *et al.*, 2016). Here, we applied the log-ratio calibration model as described by

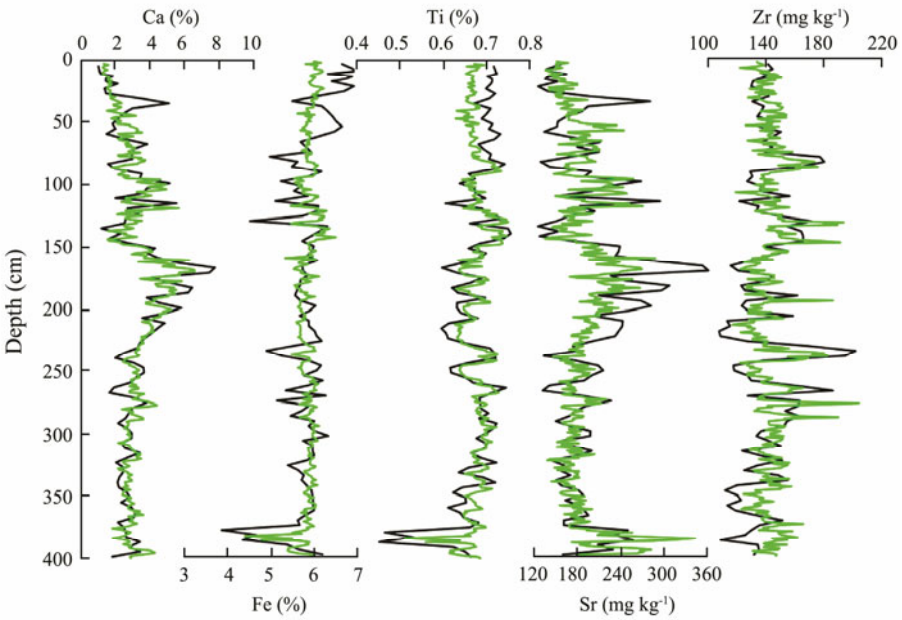

Fig.4 Comparisons of the elemental concentrations analyzed by ICP (black lines) and calculated by the XRF methods (green lines) in the sediments of core CS11.

Weltje and Tjallingii (2008) to correct these matrix effects using the following equation:

$$\ln(\frac{\bar{W}_{ij}}{\bar{W}_{id}}) = \alpha_{jd} \ln(\frac{I_{ij}}{I_{id}}) + \beta_{jd} . \quad (5)$$

Eq. (5) is the log-ratio calibration equation (LRCE), where W_{ij} and W_{id} represent the concentrations of elements j and d in specimen i, respectively; I_{ij} and I_{id} represent the scanning intensities of elements j and d in specimen i, respectively; and the parameters α and β are the model matrix effect parameter and the model detection efficiency parameter for a particular element, respectively. Considering the elemental ratios, this equation minimizes the interference from the matrix effect of sediments. The fitting degree of the predictions by this method is based on the errors in the log ratio of the content predictions. The variance estimates of the residuals of the predicted values are as follows:

$$S_{jd}^2 = med_i^{\ n} \left\{ \ln(\frac{W_{ij}}{W_{id}}) - \ln(\frac{\bar{W}_{ij}}{\bar{W}_{id}}) \right\}^2 , \quad (6)$$

by comparing S_{jd}^2 with this total variance, the fitting degree of the LRCE prediction model can be obtained according to Eq. (7):

$$\begin{cases} R_{jd}^2 = \dfrac{V_{jd} - S_{jd}^2}{V_{jd}}, \ V_{jd} > S_{jd}^2 \\ R_{jd}^2 = 0, \ V_{jd} < S_{jd}^2 \end{cases} , \quad (7)$$

where V_{jd} is the total variance in the calibrated sample measurements.

From Eq. (5), the XRF intensity ratio is theoretically linearly correlated with the content ratio as determined from conventional testing methods. After log calibration, the parameters α and β determine the functional relationship between the elemental intensity and elemental content log ratios. The matrix effect calibration parameter α and the detection efficiency parameter β are calculated according to the method proposed by Weltje and Tjallingii (2008). The contents of the major elements corresponding to the XRF scanning were tested and then solved by a major axis regression analysis (Weltje and Tjallingii, 2008; Boyle *et al.*, 2015; Pang *et al.*, 2016). The coefficients α and β for the 12 elements obtained from core CS11 are shown in Tables 2 and 3. The optimal parameters α and β were generally selected according to the degree of fit between the predicted and measured elemental contents (Pang *et al.*, 2016).

Table 4 lists the fitting degree R^2 between the log ratios of the elements. When different elements are used for comparisons and when Ca is used as the calibration denominator, the fitting degree R^2 (interpreted as the relative of the signal represented by the down-core variability of the predicted log-ratio concentrations) between elements is the highest. Hence, Ca was used as the LRCE calibration denominator. As shown in Table 4, ln(K/Ca) has the highest R^2 value. By choosing the corresponding optimal matrix effect parameter α and detection efficiency parameter β in Tables 2 and 3, we can establish the expression for converting the intensity to the elemental content, as shown in Eq. (8):

$$\ln(\frac{\bar{W}_{\mathrm{K}}}{\bar{W}_{\mathrm{Ca}}}) = 0.5544 \times (\frac{I_{\mathrm{K}}}{I_{\mathrm{Ca}}}) + 0.2022 . \quad (8)$$

The expression for converting the elements with rela-

Table 2 Model matrix effect parameters α for the 12-element composition of the sediments from core CS11

α	Al	K	Ca	Ti	Mn	Fe	Ni	Cu	Zn	Rb	Sr	Zr
Al	0	2.637	2.968	1.332	0.553	5.619	0.990	0.938	0.085	3.482	2.723	4.546
K	2.637	0	0.554	4.998	1.748	0.914	1.893	0.926	1.213	1.010	0.835	1.001
Ca	2.965	0.554	0	1.858	1.417	1.330	2.043	2.215	1.335	1.130	0.940	1.116
Ti	1.332	4.998	1.858	0	1.132	1.997	1.209	0.943	0.826	0.678	0.572	0.681
Mn	0.553	1.748	1.417	1.132	0	1.491	0.628	0.717	0.410	0.297	0.236	0.306
Fe	5.619	0.914	1.330	1.997	1.491	0	2.888	0.727	1.772	1.522	1.251	1.489
Ni	0.990	1.893	2.043	1.209	0.628	2.888	0	1.035	0.710	0.434	0.572	0.546
Cu	0.938	0.926	2.215	0.943	0.717	0.727	1.035	0	1.557	1.380	1.544	1.479
Zn	0.085	1.213	1.335	0.826	0.410	1.772	0.710	1.557	0	180.949	0.386	0.243
Rb	3.482	1.010	1.130	0.678	0.297	1.522	0.434	1.380	180.949	0	1.023	70.449
Sr	2.723	0.835	0.940	0.572	0.236	1.251	0.572	1.544	0.386	1.023	0	0.632
Zr	4.546	1.001	1.116	0.681	0.306	1.489	0.546	1.479	0.243	70.449	0.632	0

Table 3 Model detection efficiency parameters β for the 12-element composition of the sediments from core CS11

β	Al	K	Ca	Ti	Mn	Fe	Ni	Cu	Zn	Rb	Sr	Zr
Al	0	−13.246	−15.872	−8.562	−6.181	−30.087	2.416	2.826	2.123	0.020	0.048	0.056
K	13.246	0	−0.202	−0.015	0.016	0.008	13.422	8.543	9.318	7.593	7.088	7.824
Ca	15.872	0.202	0	−0.164	−0.004	0.195	15.065	17.153	10.399	8.488	7.812	8.708
Ti	8.562	0.015	0.164	0	0.034	0.003	10.722	9.806	8.740	7.566	7.432	7.804
Mn	6.181	−0.016	0.004	−0.034	0	−0.014	8.379	9.076	7.991	7.427	7.648	7.643
Fe	−30.087	−0.008	−0.195	−0.003	0.014	0	20.498	7.191	12.553	10.013	8.800	10.182
Ni	−2.416	−13.422	−15.065	−10.722	−8.379	−20.498	0	0.525	0.140	0.056	0.055	0.075
Cu	−2.826	−8.543	−17.153	−9.806	−9.076	−7.191	−0.525	0	−1.450	−2.677	−2.640	−2.175
Zn	−2.123	−9.318	−10.399	−8.740	−7.991	−12.553	−0.140	1.450	0	−140.694	−0.016	−0.022
Rb	−0.020	−7.593	−8.488	−7.566	−7.427	−10.013	−0.056	2.677	140.694	0	0.100	8.206
Sr	−0.048	−7.088	−7.812	−7.432	−7.648	−8.800	−0.055	2.640	0.016	−0.100	0	0.003
Zr	−0.056	−7.824	−8.708	−7.804	−7.643	−10.182	−0.075	2.175	0.022	8.206	−0.003	0

Table 4 Goodness-of-fit statistics (R^2) of the measured log-ratio concentrations ('reference value') and log-ratio concentrations predicted from the scanning XRF results

R^2	Al	K	Ca	Ti	Mn	Fe	Ni	Cu	Zn	Rb	Sr	Zr
Al	0	0.094	0.568	0.032	0.287	0.232	0.217	0.207	0.161	0.012	0.303	0.103
K	0.094	0	0.607	0.215	0.293	0.292	0.183	0.119	0.219	0.003	0.507	0.274
Ca	0.568	0.607	0	0.599	0.517	0.598	0.126	0.525	0.540	0.512	0.410	0.580
Ti	0.032	0.215	0.599	0	0.263	0.450	0.188	0.002	0.171	0	0.535	0.250
Mn	0.287	0.293	0.517	0.263	0	0.125	0.069	0.006	0.162	0.192	0.386	0.237
Fe	0.232	0.292	0.589	0.450	0.125	0	0.176	0.004	0.117	0.031	0.496	0.326
Ni	0.217	0.183	0.126	0.188	0.069	0.176	0	0.125	0.096	0.149	0.042	0.286
Cu	0.130	0.119	0.525	0.109	0.006	0.074	0.125	0	0.099	0.134	0.322	0.139
Zn	0.161	0.219	0.540	0.171	0.162	0.117	0.096	0.099	0	0.077	0.413	0.284
Rb	0.012	0.003	0.572	0	0.192	0.031	0.149	0.134	0.077	0	0.536	0.212
Sr	0.303	0.507	0.405	0.535	0.386	0.496	0.042	0.322	0.413	0.536	0	0.546
Zr	0.103	0.274	0.580	0.250	0.237	0.326	0.286	0.139	0.284	0.212	0.546	0

tively high R^2 values, namely, Ti, Fe, and Zr, could also be obtained. As shown in Fig.5, the calibrated values of the elements with relatively high degrees of fit clearly agree well with the measured values. Hence, the intensity log ratios between the different elements and Ca can be converted to the content log ratios between these elements and Ca.

6 Conclusions

By comparing the sediment elemental results for core CS11 in the South China Sea deep basin using XRF scanning with the ICP test methods, we can draw the following conclusions:

1) The analyzed elements can be roughly separated into three classes: Class I includes elements with high correlation coefficients, such as Ca, Sr, and Zr; Class II includes elements with moderate correlations, such as Fe, Mn, Ti, and Cu; and Class III consists of elements with low correlations, such as K, Ni, Zn, Rb, and Al.

2) In the deep-sea context of the South China Sea, pore water, compaction, and particle size have little influence on the elemental results of short core sediments. Hence, the elements with good correlation coefficients may be

selected to directly convert the XRF intensities to elemental contents using a least-squares method. The converted contents generally agree with the ICP measurements.

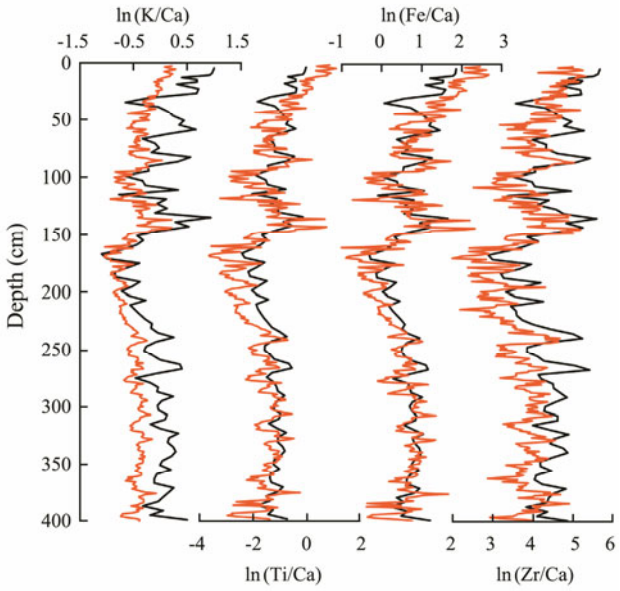

Fig.5 Comparison of the measured (black lines) and predicted log-ratio element concentrations from the XRF data (orange lines) of sediment core CS11.

3) A log-ratio calibration model was established. Using Ca as the calibration denominator, the ln(K/Ca), ln(Ti/Ca), ln(Fe/Ca), and ln(Zr/Ca) values show the same variation trends as the measured curves.

Acknowledgements

We would like to thank the anonymous reviewers for their constructive reviews of the earlier versions of this paper. This study was jointly supported by the National Natural Science Foundation of China (Nos. 41576058 and 41976192), the Project of China Geological Survey (No. DD20191010), the Shandong Provincial Natural Science Foundation of China (No. ZR2020MD061), the Open Foundation of the State Key Laboratory of Loess and Quaternary Geology (Nos. SKLLQG1707 and SKLLQG1805), and the Strategic Priority Research Program of Chinese Academy of Sciences (No. XDB40000000).

References

Boyle, J., Chiverrell, R., and Schillereff, D., 2015. Approaches to water content correction and calibration for µXRF core scanning: Comparing X-ray scattering with simple regression of elemental concentrations. In: *Micro-XRF Studies of Sediment Cores*. Croudace, I., and Rothwell, R., eds., Springer, Dordrecht, 373-390.

Chen, Q., Kissel, C., Govin, A., Liu, Z. F., and Xie, X., 2016. Correction of interstitial water changes in calibration methods applied to XRF core-scanning major elements in long sediment cores: Case study from the South China Sea. *Geochemistry, Geophysics, Geosystems*, **17** (5): 1925-1934.

Croudace, I. W., and Williams-Thorpe, O., 1988. A low dilution, wavelength-dispersive X-ray fluorescence procedure for the analysis of archaeological rock artefacts. *Archaeometry*, **30** (2): 227-236.

Croudace, I. W., Rindby, A., and Rothwell, R. G., 2006. ITRAX: description and evaluation of a new multi-function X-ray core scanner. *Geological Society, London, Special Publications*, **267** (1): 51-63.

Gao, S., Liu, Y., Yang, Y., Liu, P. J., Zhang, Y. Z., and Wang, Y. P., 2015. Evolution status of the distal mud deposit associated with the Pearl River, northern South China Sea continental shelf. *Journal of Asian Earth Sciences*, **114** (3): 562-573.

Ge, L., Lai, W., and Lin, Y., 2005. Influence of and correction for moisture in rocks, soils and sediments on *in situ* XRF analysis. *X-Ray Spectrometry*, **34** (1): 28-34.

Haschke, M., 2006. The Eagle III BKA system, a novel sediment core X-ray fluorescence analyser with very high spatial resolution. *Geological Society, London, Special Publications*, **267** (1): 31-37.

Hennekam, R., and de Lange, G., 2012. X-ray fluorescence core scanning of wet marine sediments: Methods to improve quality and reproducibility of high-resolution paleoenvironmental records. *Limnology and Oceanography: Methods*, **10** (12): 991-1003.

Jansen, J. H. F., Van der Gaast, S. J., Koster, B., and Vaars, A. J., 1998. CORTEX, a shipboard XRF-scanner for element analyses in split sediment cores. *Marine Geology*, **151** (1-4): 143-153.

Janssens, K., Vittiglio, G., Deraedt, I., Aerts, A., Vekemans, B., Vincze, L., *et al*., 2000. Use of microscopic XRF for non-destructive analysis in art and archaeometry. *X-Ray Spectrometry*, **29** (1): 73-91.

Kido, Y., Koshikawa, T., and Tada, R., 2006. Rapid and quantitative major element analysis method for wet fine-grained sediments using an XRF microscanner. *Marine Geology*, **229** (3-4): 209-225.

Kuhlmann, H., Freudenthal, T., Helmke, P., and Meggers, H., 2004. Reconstruction of paleoceanography off NW Africa during the last 40000 years: Influence of local and regional factors on sediment accumulation. *Marine Geology*, **207** (1-4): 209-224.

Lei, G. L., Zhang, H. C., Chang, F. Q., Zhu, Y., Li, C. H., Xie, X., *et al*., 2011. Comparison and correction of element measurements in lacustrine sediments using X-ray fluorescence core-scanning with ICP-OES method: A case study of Zigetang Co. *Journal of Lake Sciences*, **23** (2): 287-294 (in Chinese with English abstract).

Liang, L. J., Sun, H., Yao, Z. Q., Liu, Y. G., and Wu, F., 2012. Evaluation of high-resolution elemental analyses of Chinese loess deposits measured by X-ray fluorescence core scanner. *CATENA*, **92**: 75-82.

Liu, X., Rendle-Bühring, R., and Henrich, R., 2017a. Geochemical composition of Tanzanian shelf sediments indicates Holocene climatic and sea-level changes. *Quaternary Research*, **87** (3): 442-454.

Liu, X., Rendle-Bühring, R., and Henrich, R., 2018. High-and low-latitude forcing of the East African climate since the LGM: Inferred from the elemental composition of marine sediments off Tanzania. *Quaternary Science Reviews*, **196**: 124-136.

Liu, X., Rendle-Bühring, R., Kuhlmann, H., and Li, A., 2017b. Two phases of the Holocene East African humid period: Inferred from a high-resolution geochemical record off Tanzania. *Earth and Planetary Science Letters*, **460**: 123-134.

Liu, Z. F., Zhao, Y. L., Colin, C., Stattegger, K., Wiesner, M. G.,

Huh, C. A., *et al*., 2016. Source-to-sink transport processes of fluvial sediments in the South China Sea. *Earth-Science Reviews*, **153**: 238-273.

Löwemark, L., Chen, H. F., Yang, T. N., Kylander, M., Yu, E. F., Hsu, Y. W., *et al*., 2011. Normalizing XRF-scanner data: A cautionary note on the interpretation of high-resolution records from organic-rich lakes. *Journal of Asian Earth Sciences*, **40** (6): 1250-1256.

Lyle, M., Lyle, A. O., Gorgas, T., Holboum, A., Westerhold, T., Hathorne, E., *et al*., 2012. Data report: Raw and normalized elemental data along the Site U1338 splice from X-ray fluorescence scanning. *Proceedings of the Integrated Ocean Drilling Program*, **320/321**: 1-19.

Norris, R. D., and Röhl, U., 1999. Carbon cycling and chronology of climate warming during the Palaeocene/Eocene transition. *Nature*, **401** (6755): 775-778.

Pang, H. L., Gao, H. S., Liu, X. P., Tian, W. Q., Zou, Y., and Pan, B. T., 2016. Preliminary study on calibration of X-ray fluorescence core scanner for quantitative element records in the Yellow River sediments. *Quaternary Sciences*, **36** (1): 237-246 (in Chinese with English abstract).

Philipp, B., Bard, E., and Rose, J., 2007. Toward direct, micron-scale XRF elemental maps and quantitative profiles of wet marine sediments. *Geochemistry, Geophysics, Geosystems*, **8**: Q05004, DOI: 10.1029/2006GC001480.

Richter, T. O., van der Gaast, S., Koster, B., Vaars, A., Gieles, R., de Stigter, H. C., *et al*., 2006. The Avaatech XRF core scanner: Technical description and applications to NE Atlantic sediments. *Geological Society, London, Special Publications*, **267** (1): 39-50.

Tjallingii, R., Röhl, U., Kölling, M., and Bickert, T., 2007. Influence of the water content on X-ray fluorescence core-scanning measurements in soft marine sediments. *Geochemistry, Geophysics, Geosystems*, **8**: Q02004, DOI: 10.1029/2006GC001393.

Wan, S. M., Li, A. C., Clift, P. D., and Jiang, H. Y., 2006. Development of the East Asian summer monsoon: Evidence from the sediment record in the South China Sea since 8.5 Ma. *Palaeogeography, Palaeoclimatology, Palaeoecology*, **241** (1): 139-159.

Wang, P. X., Li, Q. Y., and Tian, J., 2014. Pleistocene paleoceanography of the South China Sea: Progress over the past 20 years. *Marine Geology*, **352**: 381-396.

Wei, G. J., Liu, Y., Li, X. H., Shao, L., and Fang, D. Y., 2004. Major and trace element variations of the sediments at ODP Site 1144, South China Sea, during the last 230 ka and their paleoclimate implications. *Palaeogeography, Palaeoclimatology, Palaeoecology*, **212** (3-4): 331-342.

Weltje, G. J., and Tjallingii, R., 2008. Calibration of XRF core scanners for quantitative geochemical logging of sediment cores: Theory and application. *Earth and Planetary Science Letters*, **274** (3-4): 423-438.

Yao, Z. Q., Liu, Y. G., Wang, K. S., and Shi, X. F., 2010. Millennial-scale paleoenvironment change during the last glacial period recorded by geochemical variations in the Japan Sea. *Bulletin of Mineralogy, Petrology and Geochemistry*, **29** (2): 119-126 (in Chinese with English abstract).

Zhang, X. L., Fan, D. J., Wang, L., Liao, Y. J., and Yao, Z. Q., 2013. The calibration and quality evaluation of elemental analysis results of marine sediment measured by an X-ray fluorescence core scanner. *Acta Oceanologica Sinica*, **35** (6): 86-95 (in Chinese with English abstract).

Zhou, R., Li, Z., Song, B., Xie, X., Li, Z., and Lu, A. Q., 2013. Reliability analysis of X-ray fluoresscence core-scanning in the Yangtze River Delta limnetic sediments. *Quaternary Sciences*, **33** (4): 697-704 (in Chinese with English abstract).

Zhu, S. Q., and Xu, G. X., 2003. A catastrophe series evaluation model of financial situation of listed companies and its empirical study. *Statistics & Information Tribune*, **18** (3): 11-14 (in Chinese with English abstract).

(Edited by Chen Wenwen)